Analysis of Residual Stresses and Dislocation Density of AA6082 Butt Welds Produced by Friction Sir Welding

ALEKSANDRA LASKA, MAREK SZKODO, PASQUALE CAVALIERE,
DOROTA MOSZCZYŃSKA, and JAROSŁAW MIZERA

The Friction Stir Welding (FSW) method was employed to join AA6082 sheets. The welds were produced with different tool traverse speed (200 and 250 mm/min), rotational speed (1000 and 1250 RPM) and tool tilt angle (0 and 2 deg). Based on the analysis of XRD patterns, the total precipitation volume fractions in the nugget zones and the base material were calculated. The FSW process resulted in a reduction in the fraction of precipitates up to 64 pct compared to the parent material. Based on the Williamson–Hall analysis and indentation tests, the residual stresses were calculated. The highest tensile residual stresses of $-$ 89.09 $\pm$ 6.19 MPa were observed for the base material, and the welding process reduced the residual stresses. The calculated dislocation density in the parent material AA6082 was equal to 8.225×10^{13} m^{-2}, while in the welds a decrease was observed up to the value of 1.419×10^{13} m^{-2}. In addition, the FSW process changed the nature of dislocations with edge-type dislocations dominating, while screw dominating character of dislocations were prevalent in the parent material. The mobility of dislocations in the studied welds was higher and reached the value of $16.78 \times 10^{-7}\frac{m}{s}$, while the dislocation mobility in the parent material was equal to 3.19×10^{-7} $\frac{m}{s}$. Process parameters during welding have a crucial effect on the amount of heat and strains introduced during the process, and thus influence the residual stresses, dislocation density and mobility, which might have a fundamental impact on the properties of the produced welds.

https://doi.org/10.1007/s11661-022-06862-4

I. INTRODUCTION

FRICTION Stir Welding (FSW), patented exactly 3 decades ago, is one of the most developed methods of joining materials. The process is based on the plasticizing of the material in the weld zone and mixing it to join the components.[1] For this purpose, a specially designed tool consisting of two essential parts—a pin and a shoulder is used. The tool, set in a rotary motion and placed between components in contact with each other, moves along the weld line. The most important role of the shoulder is to generate heat that plasticizes the material through between its surface and the workpiece.[2] The pin, meanwhile, mixes the plasticized material, creating the weld.[3] The most important process parameters include the tool's traverse and rotational speed, the geometry of the tool and tool tilt angle.[4]

The FSW process produces a fine-grained structure in the nugget zone as a result of dynamic recrystallization in the weld.[5–7] Numbers of studies have been conducted to investigate recrystallization phenomena during the FSW of aluminum alloys.[8–10] The microstructural evolution during the process depends mostly on the temperature and strain evolution having a significant influence on the mechanical and electrochemical properties of aluminum alloys.[11] Also, the precipitate dissolution and coarsening at high temperatures during the FSW process lead to significant changes in the properties of the welded samples.[12,13] Another factor that has a significant impact on material properties is the density and type of dislocations evolving during the process. To understand the microscopic process of plastic behavior of the material, studies of dislocation density and mobility are necessary. Dislocation density and the velocity of dislocations influence the mechanical

---

ALEKSANDRA LASKA and MAREK SZKODO are with the Faculty of Mechanical Engineering and Ship Technology, Gdansk University of Technology, Narutowicza 11/12, 80-233 Gdańsk, Poland. Contact e-mail: aleksandra.laska@pg.edu.pl PASQUALE CAVALIERE is with the Department of Innovation Engineering, University of Salento, Via per Arnesano, 73100 Lecce, Italy. DOROTA MOSZCZYŃSKA and JAROSŁAW MIZERA Faculty of Materials Science and Engineering, Warsaw University of Technology, Woloska 141, 02-507 Warsaw, Poland.
Manuscript submitted July 13, 2022; accepted October 14, 2022.

properties and the hardness of the material.[14] Lower dislocation mobility and high dislocation density result in an enhanced strength of the material.[15] Dislocation density is closely related to the straining resulting from severe plastic deformation and recrystallization during the friction stir welding process.[16,17] Woo *et al.*[18] noted that for FSW AA6061-T6 aluminum joints the dynamic recrystallized zone of the weld exhibits a low dislocation density compared to the parent material. In other studies by Woo *et al.*,[19] an increase in the dislocation density in the nugget zone was revealed in FSW AA6061-T6 joints. In Reference [20], Yuzbekova *et al.* noted an increase in the dislocation density in FSWed AA5024 aluminum alloy, compared to the base metal. Lee *et al.*[21] found lower dislocation density in the weld nugget of friction stir welded copper. In the study, it was also concluded that the hardness of the weld strongly depends on the dislocation density, rather than the grain size. The limited number of studies conducted in this area and the above assumption keep the topic addressed timely and relevant to the assessment of the strength of the joint.

Residual stress is another factor strongly affecting the mechanical properties of the welds. Residual stresses in the joints have a significant influence on its fatigue properties, and consequently on the lifetime of the welded component.[22] Tensile residual stresses, unlike compressive residual stresses, increase the negative effect of the environment. Residual stresses present in material might induce environmentally assisted cracking, as well as increased fatigue crack initiation susceptibility.[23] Moreover, the significant intensification of stress corrosion cracking can be observed at tensile residual stresses.[24] During the FSW process, the material in the nugget zone is both tensiled and compressed by friction and, at the same time, is exposed to the thermal compressive stresses due to the heat input.[25] Also, the corrosion resistance of materials may depend on the residual stresses and dislocations present in the material.[26,27] In the studies of Peel *et al.*[28] synchrotron analysis of residual stresses in AA5083 FSWed joints revealed the tension character of stresses in both parallel and perpendicular directions to the tool traverse direction. Also, the tool traverse speed strongly influences residual stresses due to the heat input and the increase of stresses is a result of a steeper thermal gradient during welding, while higher traverse speeds are applied. John *et al.*[29] investigated the effect of residual stresses on the fatigue crack growth in FSWed AA7050 alloy. It was revealed that even low residual stresses induced in the welds during the process resulted in significantly affected fatigue crack growth. In the studies of Steuwer *et al.*[30], the significant tensile residual stresses were found in the gion around the weld line of dissimilar AA5083/ A6082 friction stir welded joints. Also, it was revealed at both tool rotational speed and traverse speed fluence the residual stresses formation. In the welds roduced by Zhang *et al.*,[31] the residual stresses bserved in 5A06 aluminum alloy and pure copper issimilar welds were too high to achieve sound and liable joints.

The Williamson–Hall analysis is a procedure that allows to calculate the crystallite size and residual stresses in the materials derived from X-ray diffraction patterns, whereas the dislocation density and its type can be calculated using the modified Williamson–Hall method.[32] Although many papers discussed the mechanical and electrochemical properties of friction stir welded AA6082 joints, a very limited number of studies is available on residual stresses and dislocation densities in the welds. The literature review still does not allow determining the effect of specific FSW process parameters on the residual stresses and dislocation densities in the welds.

The purpose of this study was to analyze the effect of friction stir welding parameters such as tool traverse speed, tool rotational speed and its tilt angle on residual stresses, dislocation density and dislocations mobility in the weld nugget of AA6082 aluminum alloy.

II. METHODOLOGY

A. *Friction Stir Welding*

The material under investigation was AA6082 aluminum alloy, solution heat-treated and artificially aged to T651 condition. The rolled sheets of 3 mm in thickness were used to perform the FSW process. The X-ray energy dispersive spectrometer (EDS) (Edax Inc., Mahwah, NJ) was used to determine the chemical composition of the chosen material. The results are shown in Table I.

The FSW process was performed on a conventional milling machine (FU251, Friedrich Engels Kazanluk, Bulgaria). For the present studies, a hexagonal pin tool was adopted to produce butt welds. Figure 1 depicts the schematic illustration of the tool. The shoulder diameter was equal to 18 mm, the distance across the flats of the hexagonal pin was equal to 6 mm and the pin length was set to 2.5 mm. The shoulder plunge depth of 0.3 mm was adopted. The material of the hexagonal pin was 73MoV52 steel and the shoulder was made of X210Cr12 steel. The hardness of the pin and the shoulder was measured (Wilson Mechanical Instrument Co. Inc.) and was equal to 58 and 61 HRC, respectively. The range of parameters was selected to produce welds without apparent defects and material discontinuities. The employed tool traverse speed values were 200 and 250 mm/min, the tool rotational speed values 1000 and 1250 rpm and the tool tilt angles 0 and 2 deg. The designations of the samples are shown in Table II. In the table, the revolutionary pitch values, defined as the tool rotational speed divided by the traverse speed for all the samples were also presented. For further testing, the specimens were cut from the nugget zone and the native material.

B. *Material Characterization*

The metallography techniques were used to reveal the macrostructures of the welds. The samples were wet ground to the final gradation of #2000 and the polished

Table I. Chemical Composition of AA6082

	Chemical composition [Weight Percent]								
	Zn	Mg	Cr	Ti	Fe	Si	Cu	Mn	Al
AA6082	0.20	1.03	0.25	0.10	0.50	0.90	0.10	0.42	balance

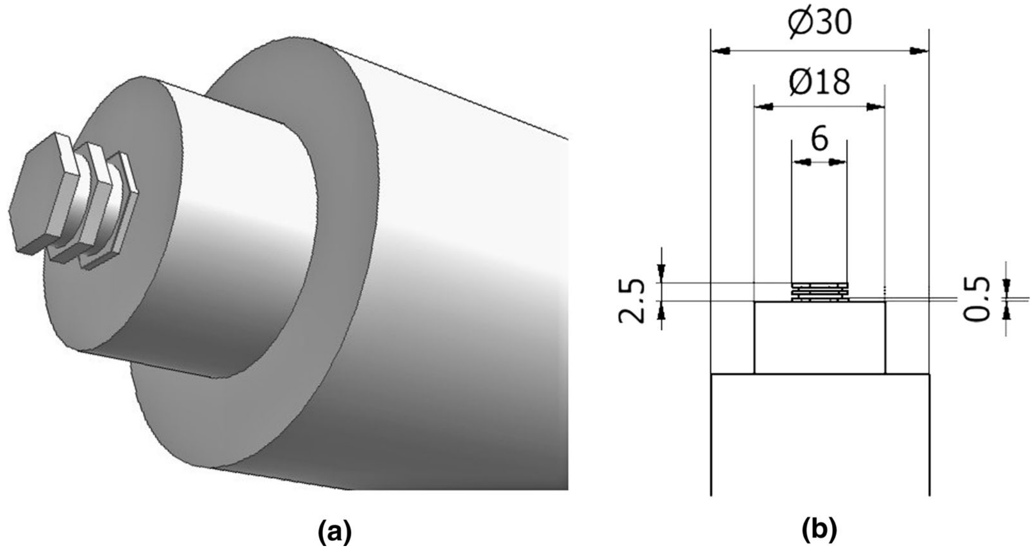

Fig. 1—Schematic illustration of the geometry of the tool used for FSW of AA6082.

Table II. Designations of the Samples

Sample	Tool Rotational Speed [RPM]	Tool Traverse Speed [mm/min]	Tool Tilt Angle [°]	Revolutionary Pitch [rot/mm]
FSW1	1000	200	0	5
FSW2	1000	250	0	4
FSW3	1250	200	0	6.25
FSW4	1250	250	0	5
FSW5	1000	200	2	5
FSW6	1000	250	2	4
FSW7	1250	200	2	6.25
FSW8	1250	250	2	5

using 1 μm diamond suspension. The polished samples were etched in a reagent consisting 1 mL HF, 1 mL HCl, 2 mL HNO_3 and 96 mL H_2O for 15 seconds. The microstructure at the cross-section of one selected weld (FSW2) was characterized by the electron backscattered diffraction (EBSD) method using a scanning electron microscope (SEM) (Hitachi SU-70, Japan). The sample for these measurements was prepared by argon ion polishing at 5 kV using Hitachi IM4000 Ion Milling System (Hitachi, Japan). The EBSD maps were taken on every zone with an acceleration voltage of 20 kV using a step size of 0.2 μm. The collected data were examined using the HKL Channel 5 (Oxford Instruments, United Kingdom) software.

The X-ray diffraction method (XRD) (Philips X'Pert Pro, Netherlands) was used via diffractometer with Cu Kα radiation with a wavelength $\lambda = 0.15418$ nm operated at 30 kV and 50 mA. The diffraction patterns were collected using Bragg–Brentano geometry over 2θ range from 20 to 90 deg with a 0.02 deg step size. To evaluate and correct the instrumental broadening effect a silicon standard was used. The Rietveld refinement method was applied for a quantitative phase analysis based on the XRD patterns using MAUD software. Mathematical procedures implemented in the Rietveld refinement approach are described in detail in the literature.[33] The Williamson–Hall analysis was used to calculate the crystallite size and microstrain in the parent material and the weld nuggets, whereas the modified Williamson–Hall analysis was applied to estimate the dislocation density. The hardness tests of the material were performed with a NanoTest Vantage nanoindenter (Nanotest Vantage, Micro Materials, United Kingdom) with a diamond Berkovich indenter. The tests were performed to determine the quantitative residual stresses in the examined samples, considering the strains calculated by the Williamson–Hall analysis and the Young's modulus obtained from the indentation tests. The samples were subjected to 10 measurements with identical parameters. The maximum force was set up at 5N, the loading and unloading time was equal to 20 seconds and the dwell period at maximum load was 5 seconds. During the measurements, the load-depth curves were recorded. Microhardness (H), reduced Young's modulus (E_{R}) and Young's modulus (E) were measured using the Oliver–Pharr method. For calculating Young's modulus from reduced Young's modulus, a Poisson's ratio equal to 0.33[34] was assumed for the analyzed samples.

III. RESULTS AND DISCUSSION

A. *Macro- and Microstructure*

Friction stir welding results in high temperatures during the process, large deformations, strains and strain rate. Figure 2 presents the macroscopic overview of the produce welds. In all the cases, a typical basin shape of the weld nugget can be observed. The uppermost part of the weld nugget is obviously wider due to the direct stirring by the tool shoulder.[35] No obvious defects were observed in the cross-sections of the joints, indicating a proper selection of the welding parameters. Moreover, a characteristic structure called "onion rings" can be observed as incomplete half elliptical bended patterns stacked into several layers. A formation of the onion ring pattern is an effect of downward and upward flow of the plasticized material around the pin while mixing. The width of the mixing zone was measured the mid-thickness of the cross-sections. It is worth to observe marginal differences in the width of the mixing zone for different process parameters. The welds produced with the tool tilt angle of 0° are characterized by slightly lower width of the stir zone. Also, for the welds produced with the tool traverse speed of 200 mm/min, the width is larger than in the case for the welds produced with the same tool tilt angle and the rotational speed, but with the tool traverse speed of 250 mm/min. This is due to the greater heat input both when the tool traverse speed is reduced and when the tool is tilted.[36,37]

High strains and heat input affect the microstructure volution not only in the mixing zone, but also in the ones not in direct contact with the tool. Accordingly, esides the base material (BM), three zones charactertic of the FSW process can be distinguished. The ugget zone (NZ) is the area experienced by direct teractions with a tool. Extreme strain and high heat put result in a dynamic recrystallization process in this ea. Due to that fact, the microstructure is very fine with equiaxed well-dispersed grains. The resulting grain size strongly depends on the thermal cycle and stirring actions. In the thermo-mechanically affected zone (TMAZ) the material is plastically deformed from shear induced by the tool and is exposed to temperature increase. The plastic deformation degree depends mostly on the exact location within the zone, with higher deformations closer to the nugget. Due to insufficient heat input, no dynamic recrystallization occurs in TMAZ. As the distance from NZ increases, the degree of plastic deformation is reduced. The heat-affected zone (HAZ) experiences only the thermal energy of the process. In the precipitation strengthened alloys, such as AA6082, the HAZ is characterized by the overaging process of the precipitates, which is a result of the drastic reduction of the mechanical properties in this zone. Determination of the boundary between HAZ and BM might be difficult based on microstructure observations. Figure 3 shows the EBSD maps with the unit triangle of the stereographic projection which displays the color code for the direction of the plane normal of the map in the crystal axes. The EBSD measurements were performed for one selected weld (FSW2) in all four zones. In the base metal of AA6082 elongated grains can be observed which is a result of the rolling of the sheets. The microstructure of HAZ exhibits slightly elongated grains, with an emerging equiaxed shape. It should be noted that the structure in HAZ is more fine-grained, compared to the native material. The shape of the grains in the TMAZ does not reflects the elongated grains observed in the parent material. Also moving nearer to the nugget zone, the material experienced higher temperatures and deformation, so the partial recrystallization process was more clearly observed, resulting in more significant grain refinement closer to the nugget zone. This can be observed on the right side of Figure 3(c). In the weld nugget, newly formed grains with regular shape and very fine structure are observed. Due to the dynamic recrystallization process, the initial inhomogeneous microstructure is replaced by the fine-grain microstructure. The nugget zone clearly exhibits the increase of $\langle 111 \rangle$ orientation. This phenomenon is the result of intense shear deformation by tool movement during the process. In[38] it was observed that at high strains, the $\langle 111 \rangle$ texture might form in fcc crystals.

B. *Precipitation Fraction Analysis*

Figure 4 presents the XRD diffraction patterns for all the tested samples. The main peaks originating from the pure aluminum with their Miller indexes are distinguished. In Figure 5 the XRD diffraction patterns of the base material and one, representative weld are presented with the peaks corresponding to the phases of the main alloying elements. In all the diffractograms, the peaks originating from the phases of Mg, Mn, Si and Fe alloying elements were visible under magnifications.

Table III presents the type and volume of precipitation and pure aluminum fractions identified on the XRD patterns. The quantitative phase analysis was performed using Rietveld refinement of the XRD patterns. The

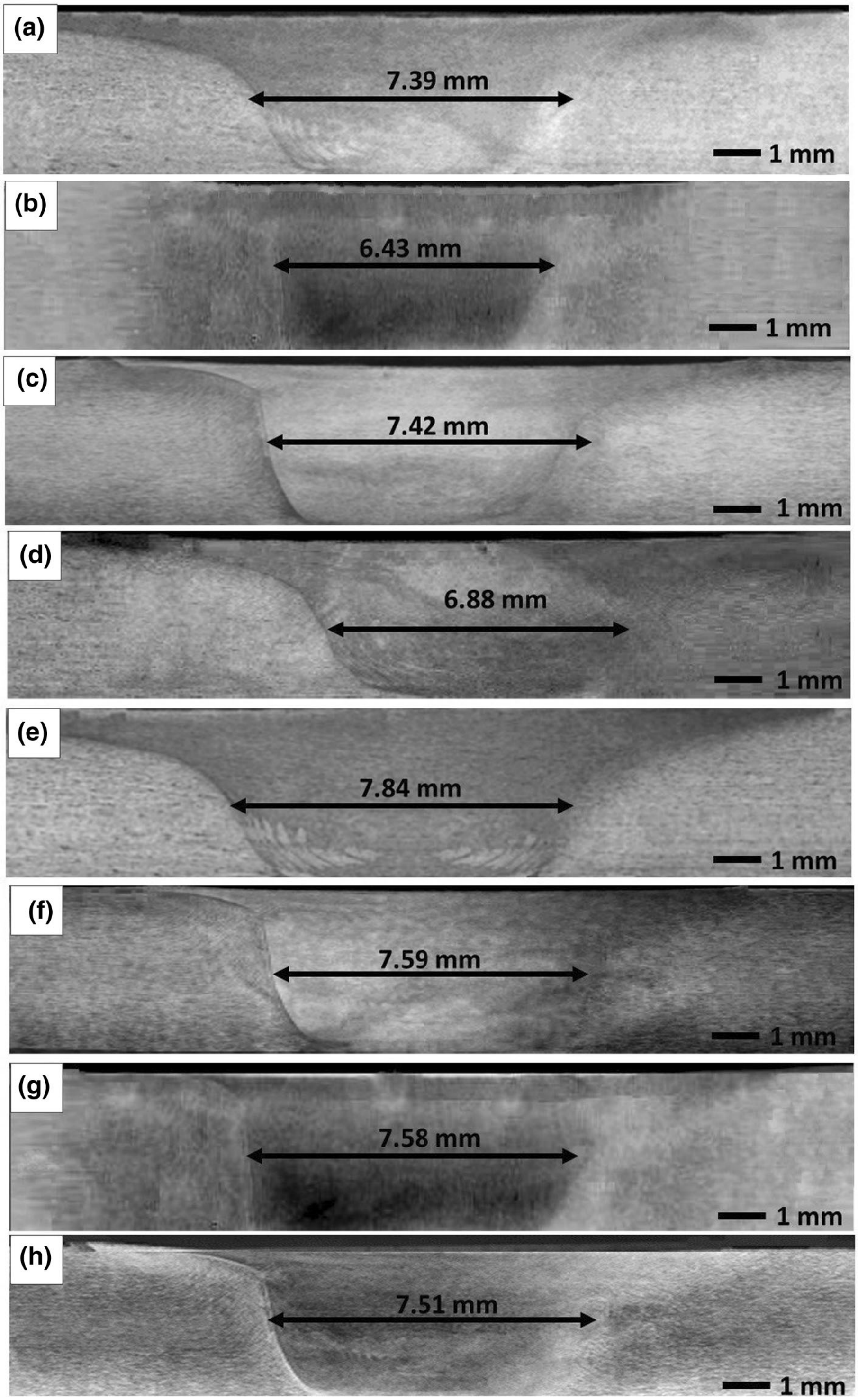

Fig. 2—Macrostructure of the produced welds—FSW1 (*a*), FSW2 (*b*), FSW3 (*c*), FSW4 (*d*), FSW5 (*e*), FSW6 (*f*), FSW7 (*g*) and FSW8 (*h*).

calculated goodness of fit values ranged from approximately 1.5 to 2.2 for all the samples, indicating very good agreement with the XRD patterns. The calculations show that the FSW process considerably reduces the precipitation content. The heat generated during the process, as well as the peak temperature, causes the dissolution of precipitates in the aluminum matrix. Aluminum alloys containing Mg and Si as the main alloying elements are precipitation hardening alloys. Small particles of precipitates strengthen the material by inhibiting the dislocation movement in the metal crystal structure.[39] The dissolution of the precipitations leads to a noticeable decrease in the hardness and strength. In the studies of Rao *et al*,[40] the dissolution of the

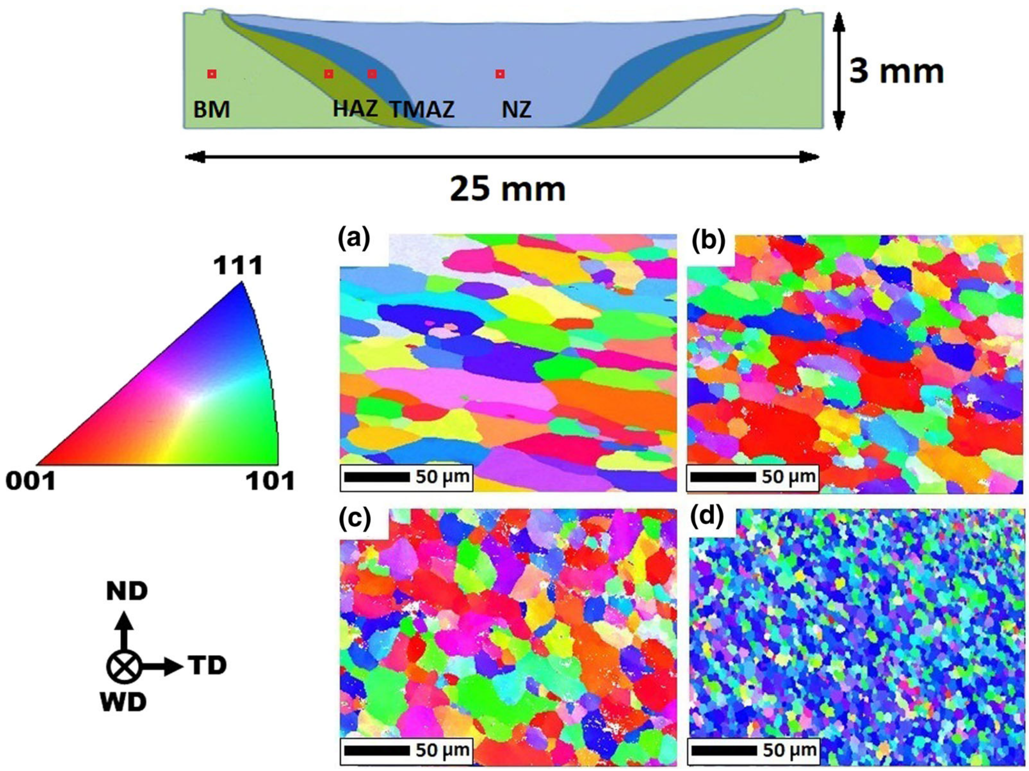

Fig. 3—EBSD maps of a selected FSW2 joint—base material AA6082 (*a*), heat-affected zone (*b*), thermo-mechanically affected zone (*c*) and weld nugget (*d*). Welding direction (WD), transverse direction (TD) and normal direction (ND) are also illustrated. The locations for the EBSD test in different zones of the FSW2 sample are also depicted.

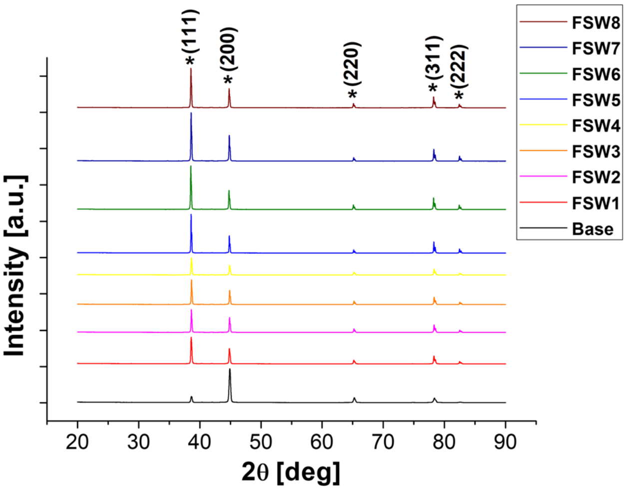

Fig. 4—Diffraction patterns for all the tested samples.

precipitates in AA2219 aluminum alloy during the FSW process was investigated. It was revealed that using a exagonal pin might lead to the dissolution of 91 pct of recipitates. Simultaneously, the use of a hexagonal pin rovides advanced material mixing, which leads to the crystallization in the weld zone and the formation of a ne-grained structure. Thus, in these studies the use of a exagonal pin resulted in an increase of the hardness of e nugget zone, compared to other pin shapes, though the precipitation dissolution was the highest. Proper mixing of the material in the weld zone during the FSW process and grain recrystallization is the basic condition for maintaining the appropriate strength of the joints. Simultaneously, the dissolution of precipitates by increasing the temperature in the process reduces the strength in the case of precipitation hardening alloys, such as AA6082.

Figure 6 presents the relationship of the total precipitation volume fraction with a respect to the revolutionary pitch for both applied tilt angles. It should be noted that using the tilt angle equal to 2 deg results in more significant precipitate dissolution, while using the non-inclined tool results in the reduction of the precipitation dissolution. For the revolutionary pitch of 4 and the tilt of 0 deg, the precipitation fraction was reduced by 48 pct compared to the base material. The maximum reduction of the precipitation fraction (almost 64 pct of reduction comparing to the base material), was noted for the revolutionary pitch equal to 6.25 and the tool tilt angle of 2 deg. While increasing the revolutionary pitch, the heat input during the welding is also increased and the precipitation dissolution is higher, which leads to the reduction of their fraction. Also, by applying the inclined tool, the heat input during the process is increased, compared to the use of the non-inclined tool. The use of an inclined tool during the FSW process increases stress on the leading edge of the tool and on the surface of the component to be welded and thus, improves the frictional heating. This leads to an increase in the temperature, which affects the more efficient

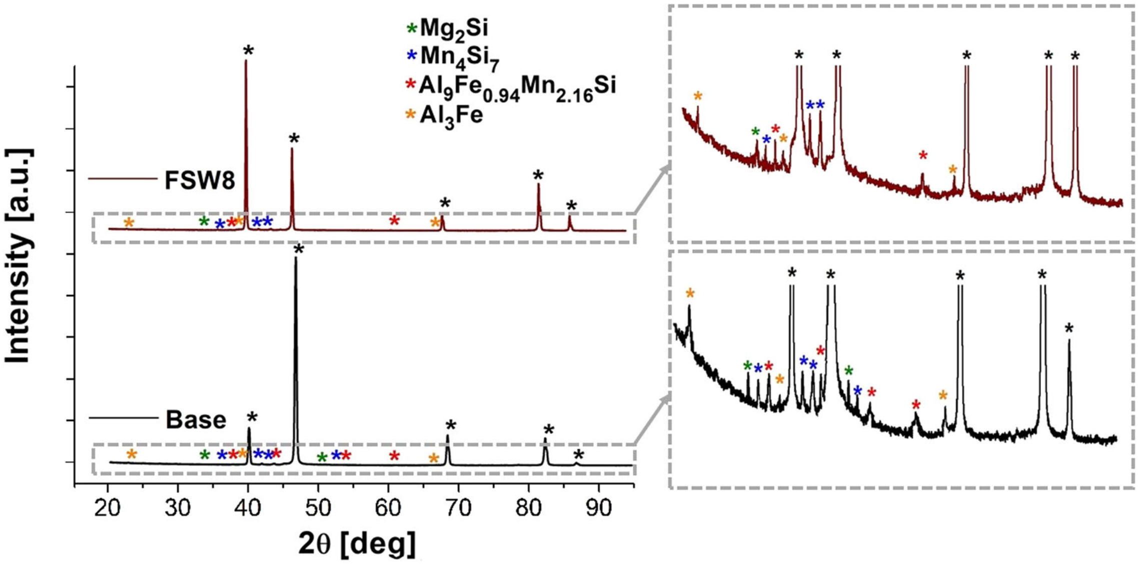

Fig. 5—Diffraction patterns of AA6082 base material and one selected weld (FSW8) with identified peaks originating from pure aluminum and phases of main alloying elements.

Table III. Type and Volume Fraction of the Precipitates Based on the XRD Patterns

	FSW1	FSW2	FSW3	FSW4	FSW5	FSW6	FSW7	FSW8	Base
Mg_2Si Percent	0.209	0.208	0.206	0.201	0.178	0.189	0.169	0.222	0.832
Mn_4Si_7 Percent	0.718	0.743	0.642	0.753	0.637	0.759	0.477	0.761	0.802
$Al_9Fe_{0.94}Mn_{2.16}Si$ Percent	0.393	0.371	0.264	0.302	0.207	0.290	0.261	0.214	0.597
Al_3Fe Percent	0.466	0.529	0.394	0.385	0.448	0.315	0.378	0.349	1.326
Precipitations Fraction Percent	1.786	1.851	1.506	1.641	1.470	1.553	1.285	1.546	3.557
Al Fraction Percent	98.214	98.149	98.494	98.359	98.530	98.447	98.715	98.454	96.443

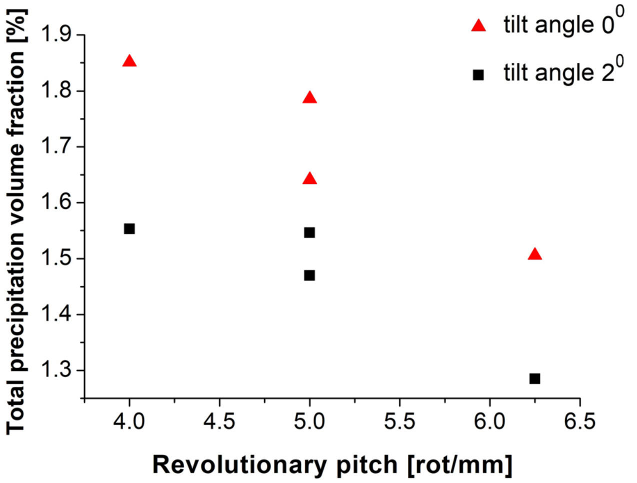

Fig. 6—Total precipitation volume fraction as a function of the revolutionary pitch for the samples produced with the tool tilt angle 0 deg (FSW1-FSW4) and 2 deg (FSW5-FSW8).

dissolution of precipitates and reduces their fraction. There are several studies on the heat input with the respect to the tool tilt angle during the FSW process. In the studies of Dialami *et al.*,[36] it was revealed that using the inclined tool results in the increase of the temperature during the process and enhances the material stirring. Krishna *et al.*[41] noted that the heat input during welding is a non-uniform function of the tilt angle, but the use of the inclined tool results in higher heat input and better plasticizing of the material. Also, Meshram *et al.*[42] observed that when a tool tilt angle of 2 deg is set during the FSW process, the highest temperature is noted on both advancing and retreating sides. Figure 6 shows that for the welds produced with the tool tilt angle of 0 deg higher values of precipitation fractions are observed for all the studied revolutionary pitch values, compared to the welds produced with the inclined tool.

C. *Residual Stresses*

A peak broadening on an XRD diffraction pattern is caused by the deviation from the ideal crystal lattice. The method that allows to distinguish the different contributions of that broadening is the Williamson–Hall analysis. This method assumes that a peak profile is a convolution of the profiles resulting from microstrains and crystallite size contributions[43]:

$$\beta_T = \beta_D + \beta_\varepsilon, \quad [1]$$

where β_T is a total broadening, β_D is a broadening resulting from the crystallite size and β_ε—from the microstrains.

The Scherrer equation presumes that the broadening due to the crystallite size can be presented as follows:

$$\beta_D = \frac{a_s \cdot \lambda}{L \cdot \cos\theta}, \quad [2]$$

where a_s is a Scherrer constant that depends on the crystal size distribution and its shape (here assumed to be equal to 1),[44] λ is the length of electron beam wave (here equal to 0.15418 nm) and L is the crystallite size that represents a crystallite portion with the same crystallographic orientation such as sub-grains (in nm).[45]

Also, the broadening due to the microstrains is defined as:

$$\beta_\varepsilon = 4\varepsilon\tan\theta, \quad [3]$$

where ε is the microstrain.

The Williamson–Hall equation, assuming the presented equations, can be defined as:

$$B = \frac{a_s \cdot \lambda}{L \cdot \cos\theta} + 4\varepsilon\tan\theta. \quad [4]$$

Or, while multiplied by cosθ, takes a form of a linear function:

$$B\cos\theta = \frac{\mathrm{a_s} \cdot \lambda}{\mathrm{L}} + 4\varepsilon\sin\theta. \quad [5]$$

Figure 7 depicts the plot of $B\cos\theta$ vs. sinθ. Also, the approximations to the linear functions were calculated for the obtained values. Based on the constants of the linear functions, according to the Eq. [5] the crystallite size and microstrains were calculated. The obtained values are presented in Table IV. In order to calculate residual stresses (σ_R) present in the material, the indentation tests were performed. Figure 8 presents hysteresis plots of load-deformation during the tests for all the samples. The Young's modulus, calculated from the obtained values of reduced Young's modulus, as well as microhardness values are also presented in Table IV.

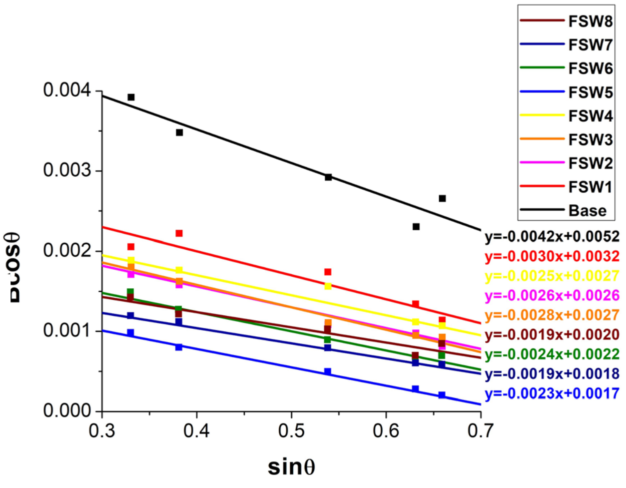

g. 7—Plots of $B\cos\theta$ vs. sinθ for all the tested samples.

It can be clearly observed that the FSW process results in the increase of the crystallite size. By applying the tilt angle of 2 deg the increment is higher than in the case of the use of the non-tilted tool. The FSW method results in a large strain in the metal matrix during welding. The heat input and, consequently, the increase of the temperature in the weld nugget results in the recrystallization and grain refinement and, simultaneously, the increase in the size of crystallites. By applying the inclined tool, the heat input is higher[36, 42] and the crystallite size increment is greater. In all the cases, the Williamson–Hall analysis revealed that the strains present in the material are below zero, which indicates their tensile nature. The calculations of residual stresses show that the base material exhibit the lowest value. It means that in the case of the AA6082 alloy, the greatest tensile nature is observed. Also in the case of all the welds, the tensile residual stresses are observed, but the values are closer to zero. Residual stresses in friction stir welded joints are the result of complex interactions during the process, including thermal, mechanical and metallurgical phenomena. Indentation tests revealed that in the nugget zone of all the produced welds the hardness values were lower than in the case of the base material. High heat input and temperature peak during the process lead to the dissolution of precipitates in the aluminum matrix, as is shown in Table III. A decrease in the amount of precipitates, which in the case of precipitation-hardened alloys inhibit the movement of dislocations in the metal crystal structure, has a direct effect on the decrease in hardness, which can be seen in the results of indentation tests.

D. *Dislocation Density and Mobility*

The modified Williamson–Hall (MWH) analysis is a method that allows the dislocation density measurements based on XRD diffraction patterns. XRD diffraction patterns of all the tested samples with a horizontal axis determined as a diffraction vector K are presented in Figure 9. The diffraction vector can be calculated as:

$$K = \frac{2\sin\theta}{\lambda}. \quad [6]$$

The modified Williamson–Hall equation can be expressed as follows:

$$\Delta K \cong \frac{a_s}{L} + bM\sqrt{\frac{\pi}{2}}\rho(K\overline{C}^{\frac{1}{2}}), \quad [7]$$

where ΔK is defined as a peak width, b is a magnitude of the Burgers vector, M is a dislocation distribution parameter, ρ is a dislocation density and $\overline{C}$ is a scaling parameter called the average contrast factor of dislocations.[46] Equation [7] is a linear function $\Delta K =$

Table IV. **Results Obtained from the Williamson–Hall Analysis and Indentation Tests**

	L [nm]	ε [−]	E [GPa]	σ_R [MPa]	H [GPa]
Base	29.62	− 0.00105	84.85 ± 5.90	− 89.09 ± 6.19	1.19 ± 0.11
FSW1	48.00	− 0.00074	82.44 ± 5.75	− 61.00 ± 4.25	1.08 ± 0.07
FSW2	58.38	− 0.00064	80.23 ± 10.97	− 51.35 ± 7.02	1.00 ± 0.09
FSW3	57.20	− 0.00069	81.18 ± 7.09	− 56.01 ± 4.89	1.11 ± 0.08
FSW4	56.43	− 0.00061	80.34 ± 6.06	− 49.01 ± 3.70	1.05 ± 0.06
FSW5	90.27	− 0.00057	80.48 ± 5.11	− 45.88 ± 2.91	1.07 ± 0.07
FSW6	68.79	− 0.00061	80.27 ± 5.38	− 48.97 ± 3.28	1.05 ± 0.10
FSW7	83.54	− 0.00048	82.30 ± 4.89	− 39.50 ± 2.35	1.04 ± 0.08
FSW8	77.09	− 0.00046	80.59 ± 6.40	− 37.07 ± 2.94	1.10 ± 0.04

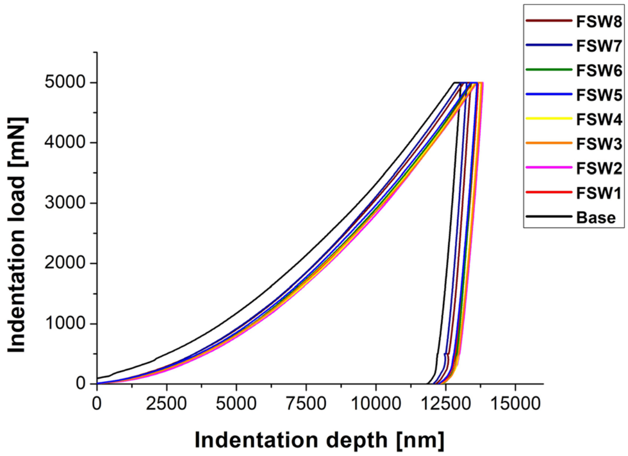

Fig. 8—Load-deformation hysteresis plots obtained during indentation tests.

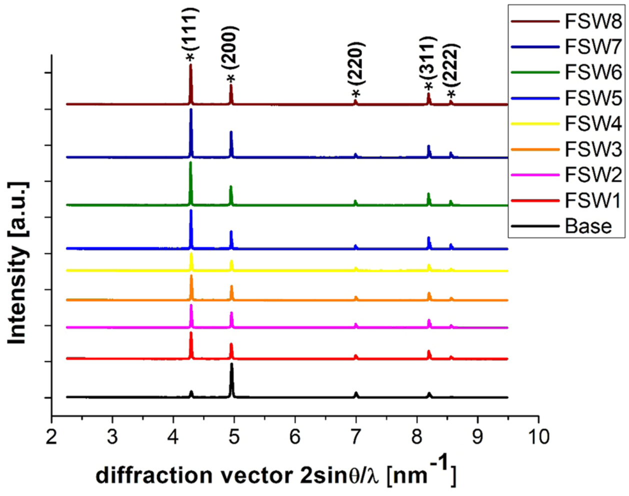

Fig. 9—Diffraction patterns for all the tested samples with a horizontal axis based on the diffraction vector K.

$f\left(K\overline{C}^{\frac{1}{2}}\right)$. The dislocation contrast factor is a function of Miller indexes and is given by:

$$\overline{C} = \overline{C}_{h00}\left(1 - qH^2\right), \qquad [8]$$

where q is a dimensionless parameter that is dependent on the edge or screw character of dislocations and H is defined as:

$$H^2 = \frac{h^2l^2 + h^2k^2 + k^2l^2}{\left(h^2 + k^2 + l^2\right)}, \qquad [9]$$

and $\overline{C}_{h00}$, is a factor of the average contrast of dislocations for {h00} reflections. It can be calculated by the dislocations contrast factor for the {h00} reflections of the pure screw and pure edge dislocation. For pure edge and pure screw dislocations, the dislocation contrast factor $\mathrm{C_{h00}}$ can be calculated as:

$$C_{h00i} = a_i^{C_{h00}}\left[1 - \exp\left(\frac{-\mathrm{A}}{\mathrm{b_i^{C_{h00}}}}\right)\right] + c_i^{c_{h00}}A + d_i^{C_{h00}}. \qquad [10]$$

Here $a_i^{C_{h00}}$, $b_i^{C_{h00}}$, $c_i^{c_{h00}}$ and $d_i^{C_{h00}}$ are parameters determined by the elastic constants of the material. The values used for the calculations are presented in Table V. According to[47] A is the elastic anisotropy parameter defined as:

$$A = \frac{2c_{44}}{c_{11} - c_{12}}. \qquad [11]$$

For the following calculations the values of c_{44}, c_{11} and c_{12} were equal to $2.83 \cdot 10^{10}$, $10.73 \cdot 10^{10}$ and $6.08 \times 10^{10}\,\frac{N}{m^2}$, according to Vallin *et al.*[48] Substitution of these values gives the elastic anisotropy parameter A equal to 1.217.

To calculate parameter q, Eqs. [7] and [8] should be combined obtaining:

$$\frac{(\Delta K - \alpha)^2}{K^2} \cong \beta^2\overline{C}_{h00}\left(1 - qH^2\right), \qquad [12]$$

where $\alpha = \frac{a_s}{L}$ and $\beta = bM\left(\frac{\pi\rho}{2}\right)^{1/2}$. The experimental value of q is determined by imposing the linear function $\frac{(\Delta K-\alpha)^2}{K^2} = f\left(K^2\right)$. The inverse value of q is obtained as the intercept of the extrapolated function with the

Table V. Parameters Needed to Calculate C_{h00} and q_i^{th} for Aluminum in fcc Crystal

	Parameter q^{th}_i [47]				Factor C_{h00}[47]			
	a^q_i	b^q_i	c^q_i	d^q_i	a^{Ch00}_i	b^{Ch00}_i	c^{Ch00}_i	d^{Ch00}_i
Screw	5.4252	0.7196	0.0690	− 3.1970	0.1740	1.9522	0.0293	0.0662
Edge*[49]	5.9049	0.8046	0.0826	− 4.374	0.2468	2.1880	0.0186	0.0731

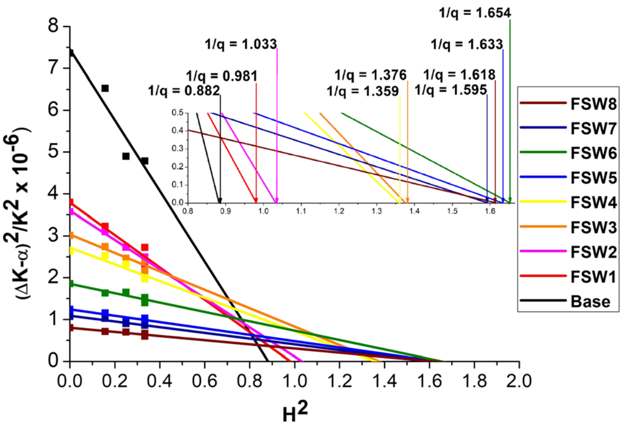

Fig. 10—Plot of Eq. [12] for all the tested samples. The intersect on the H^2 gives $1/q$.

horizontal axis. Figure 10 presents the plot of Eq. [12] and the values of $1/q$.

Based on the calculated values of q, the fraction of screw and edge character dislocations can be calculated

$$f^{edge} = \frac{q^{th}_{screw} - q}{q^{the}_{screw} - q^{th}_{edge}} = 1 - f^{screw}. \qquad [13]$$

Here f^{edge} and f^{screw} mean the fractions of each type of dislocations. To make these calculations, the theoretical values of q for the pure screw ($q^{th}{}_{screw}$) and pure edge ($q^{th}{}_{edge}$) dislocations are needed. These values can be determined based on Eq. [14]:

$$q_i^{th} = a_i^q\left[1 - \exp\left(\frac{-A}{b_i^q}\right)\right] + c_i^q A + d_i^q. \qquad [14]$$

The elastic anisotropy parameter A was calculated according to Eq. [11], while a_i^q, b_i^q, c_i^q and d_i^q are values depending on the elastic constants and dislocations slip systems activated in crystals. The parameters needed to determine q_i^{th} values are presented in Table V.

Table VI presents the calculated values of q^{th}_{screw} and q^{th}_{edge}, as well as the fractions of screw and edge type dislocations determined using Eq. [13]. Also $C_{h00screw}$, $C_{h00edge}$ and $C_{h00average}$ values are presented in Table VI.

After calculations of the q value for all the tested samples, the dislocation contrast value C^{-} is calculated according to Eq. [8]. Figure 11 presents the MWH equations plots for all the samples with the approximations to the linear functions. The results show that for all the welded samples the line broadening ΔK is less significant in each (h k l) peak than in the case of AA6082 parent material. Based on the slope of the straight lines the dislocation densities were calculated, taking the M parameter equal to 2 and the Burgers vector equal to 0.286 nm.[50] The values of dislocation densities for all the tested samples are presented in Table VII.

Due to the severe plastic deformations during the friction stir welding and recrystallization process, the dislocation density is closely related to the straining.[18] The modified Williamson–Hall analysis revealed that the highest dislocation density was found for the base material AA6082 and was equal to 8.225 × 10^{13} m^{-2}. The FSW process results in a decrease in dislocation

Table VI. The Theoretical Values of q for Screw and Edge Dislocations, the Fraction of Screw and Edge Dislocations, the Theoretical Value of Dislocation Contrast for Screw and Edge Dislocations, and the Average Dislocation Contrast Factor for the {h00} Reflections for All the Tested Samples

	$q^{th}{}_{screw}$	$q^{th}{}_{edge}$	f^{screw}	f^{edge}	$C_{h00screw}$	$C_{h00edge}$	$C_{h00average}$
base	1.313	0.331	0.818	0.182	0.183	0.200	0.186
FSW1	1.313	0.331	0.662	0.338	0.183	0.200	0.188
SW2	1.313	0.331	0.649	0.351	0.183	0.200	0.189
SW3	1.313	0.331	0.403	0.597	0.183	0.200	0.193
SW4	1.313	0.331	0.412	0.588	0.183	0.200	0.193
SW5	1.313	0.331	0.287	0.713	0.183	0.200	0.195
SW6	1.313	0.331	0.279	0.721	0.183	0.200	0.195
SW7	1.313	0.331	0.302	0.698	0.183	0.200	0.195
SW8	1.313	0.331	0.293	0.707	0.183	0.200	0.195

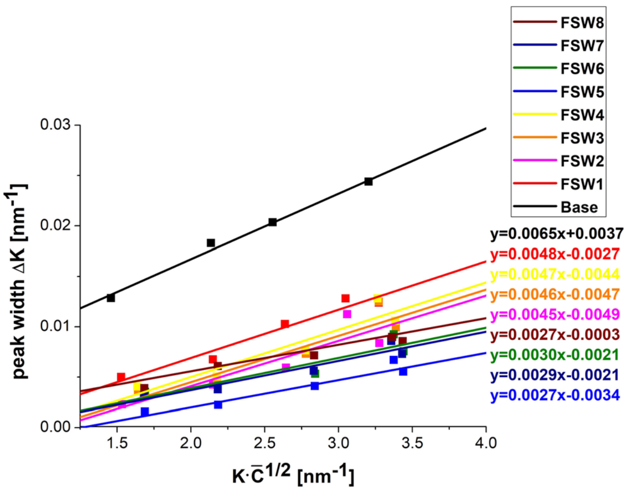

Fig. 11—The modified Williamson–Hall plot for welded samples and the parent material AA6082.

density. The analysis showed that using an inclined tool and thus increasing the amount of heat input causes a more intense decrease in dislocation density up to a value of 1.419 × 10^{13} m^{-2} for FSW5 and FSW8 samples. In the studies of Woo *et al.*,[18] it was also noted that friction stir-welded AA6061 alloy performs lower dislocation density compared to the base material in the form of as-received rolled aluminum plate. It was revealed that lower dislocation density in the nugget zone results in a high strain hardening capacity and exponent during tensile plastic deformation. In the base metal region, where the dislocation density was higher, lower strain hardening and poor ductility were found. Valvi *et al.*[51] proposed the evaluation of the dislocation density in similar AA6061 and dissimilar AA6061/AA5086 weld zones during FSW. The proposed analysis was a function of grain size and depends on strain rate, strain and temperature. It was revealed that using the analytical model gives accurate predictions and the results obtained are consistent with the studied on the welds of Woo *et al.*.[18]

To calculate the mobility of the dislocations (v), the creep of the material during the dwell time in indentation tests was studied. Figure 12 presents the relationship of strain and time. The Orowan Eq. [15] allows to calculate the dislocation velocity based on the formula:[52]

$$\frac{\mathrm{d}\varepsilon}{\mathrm{d}t} = \dot{\varepsilon} = b \cdot \rho \cdot v, \qquad [15]$$

where $\dot{\varepsilon}$ is a strain derivative. To calculate this value, the stabilized fragment of the creep was approximated to the linear function. The Orowan equation can be converted to:

$$v = \frac{\dot{\varepsilon}}{b \cdot \rho}. \qquad [16]$$

The results of the analysis strain–time relationship are presented in Table VIII.

Table VII. Dislocation Density for All the Tested Samples Calculated from the Modified Williamson–Hall Analysis

	Base	FSW1	FSW2	FSW3	FSW4	FSW5	FSW6	FSW7	FSW8
ρ [m^{-2}]	8.225 × 10^{13}	4.485 × 10^{13}	3.942 × 10^{13}	4.119 × 10^{13}	4.300 × 10^{13}	1.419 × 10^{13}	1.752 × 10^{13}	1.637 × 10^{13}	1.419 × 10^{13}

The results of the calculations based on the Orowan equations clearly indicate that the FSW process influences the dislocation mobility. The calculated velocities are higher in the case of samples welded with the tool tilt angle of 2 deg (FSW5-FSW8) than for the ones produced with the tool tilt angle equal to 0 deg (FSW1-FSW4). It should be emphasized that dislocation mobility and velocity control the mechanical behavior of the material, and the strength has a tendency to decrease as the velocity of dislocations increases. The Williamson–Hall analysis also revealed that the FSW process changes the nature of the dislocations. The native material is dominated by screw character of dislocations, accounting for almost 82 pct. An increase in edge-type dislocations was observed in all welds, up to values above 72 pct for the FSW6 sample. It should also be noted that the use of an inclined tool increases the proportion of character of dislocations from edge to screw type. This is attributed to the strains introduced into the material in various processes, such as FSW. Also, the use of an inclined tool in friction stir welding increases the strain in the material during the process. It is believed that as a result of relatively small deformations, the constriction required for cross-slip begins to become difficult, resulting in edge dislocations becoming more mobile. It leads to their annihilation while leaving screw-like dislocations. Consequently, screw character of dislocations dominate in the rolled parent material. While increasing strains, which can be observed in the FSW process, the character of dislocations changes from screw to edge. Providing greater deformation, thermally activated recovery processes result in increased annihilation of dislocations, which is suggested as cross-slip of screws. Consequently, the fraction of screw type dislocations decreases, which implies an increase in the fraction of edge character of dislocations. These observations are in agreement with the studies of Teena Mouni *et al.*[53] on type 304 steel subjected to different strain levels. Also, Schafler *et al.*[54] observed the increase of the fraction of edge dislocations under high strains in 99.9 pct Cu. On the contrary, at small strains, the dominance of the character of screw dislocations was noted, with only 10 pct of all dislocations characterized by edge character. These results are in good correspondence with the present studies. Simm[55] in the studies on compression tested 304 type steel attributed the observed decrease in q, therefore, an increase in the fraction of edge dislocations, to activation of secondary slip systems.

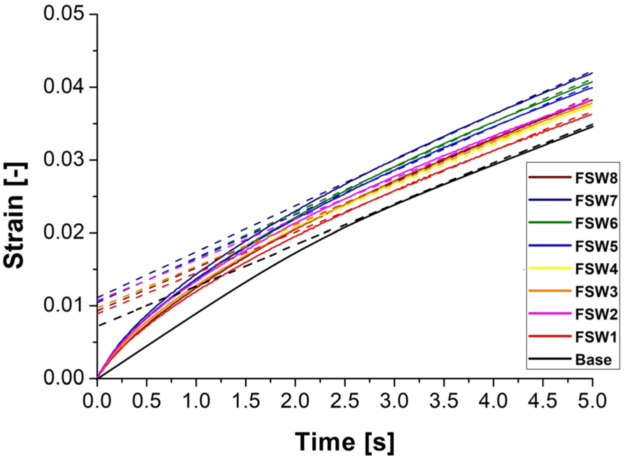

Fig. 12—Strain–time diagram for the dwell period during indentation tests.

The increase in the proportion of edge dislocations also affects their mobility. It is believed that an increase in edge-type dislocation density and a decrease in the density of screw character dislocations lead to the increase in dislocation mobility. This results in the material softening due to the particles cut and loop, as well as the increase in lattice straining. There are plenty of studies on dislocation velocity proving that dislocations with edge character domination have higher mobility than screw dislocations.[56, 57] In the studies on the FSW samples, it can be clearly seen, that by welding AA6082, the character of dislocations changes with an increase of the fraction of edge domination dislocations and thus their mobility increases, which might strongly affect the mechanical properties of the welds. Also, during the process, the precipitations dissolute and thus, the inhibition of the dislocation movement is weaken. A low number of dislocations and their high mobility, due to the precipitation dissolution and the increase of edge character of dislocations, decreases the strength of the material. Figure 13 presents the relationship of the dislocation density quotient to its mobility as a function of the revolutionary pitch for welds produced with the tool tilt angle of 0 deg (a) and 2 deg (b). The more dislocations with low mobility present in the materials, the higher strength is expected. It is clearly seen that with an increase of revolutionary pitch and thus the higher heat input, the value of this quotient is lower. Also, by using the inclined tool and increasing the heat input, the values of the quotients are lower than in the case of the non-inclined tool. Higher strains introduced in the material during welding with the inclined tool resulted in a formation of edge dislocations, characterized by higher mobility. It means that heat input and temperature peak is the main reason for decreasing the precipitation fraction and dislocation density. The reduction of the screw dominating type

Table VIII. Dislocation Mobility of the Tested Samples Based on the Indentation Tests

	Base	FSW1	FSW2	FSW3	FSW4	FSW5	FSW6	FSW7	FSW8
$[\frac{m}{s}]$	3.19×10^{-7}	4.69×10^{-7}	4.84×10^{-7}	4.37×10^{-7}	4.54×10^{-7}	13.46×10^{-7}	16.78×10^{-7}	12.38×10^{-7}	13.54×10^{-7}

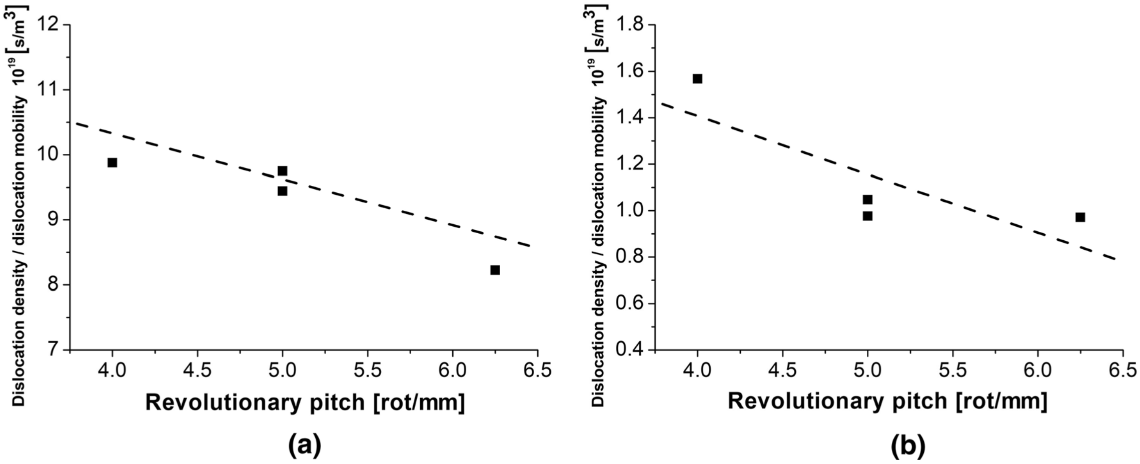

Fig. 13—The quotient of dislocation density and their mobility as a function of the revolutionary pitch for the welds produced with the tool tilt angle of 0 deg (*a*) and 2 deg (*b*).

dislocations fraction and, at the same time, the increase of the edge-type dislocation fractions are mostly influenced by the strains introduced in the material by the inclined tool. The decrease of precipitation fractions, as well as the change of the dislocations character, influenced the dislocation mobility. These relationships are clearly visible by analyzing the relationships based on revolutionary pitch, as well as comparing the values for the inclined and non-inclined tools.

IV. CONCLUSIONS

The present study focuses on the residual stresses, dislocation mobility and density of friction stir welded AA6082 aluminum alloy under different process parameters. The following conclusions can be drawn from the systematic research:

1. AA6082 aluminum alloy sheets were successfully welded using the FSW method with the tool with a hexagonal pin. Process parameters such as tool traverse speed of 200 and 250 mm/min, tool rotational speed of 1000 and 1250 RPM and tool tilt angle of 0 deg and 2 deg allowed to produce defect-free welds.
2. Typical microstructure containing elongated base material grains and fine grain weld nugget was observed by the EBSD method. Also, typical zones such as HAZ and TMAZ were found on the EBSD map.
3. Precipitation volume fractions in the nugget zones of all produced welds were calculated based on XRD patterns and Rietveld refinement. It was noted that a more significant reduction of precipitation fraction can be observed for the welds produced with a tool tilt angle of 2 deg, compared to the welds produced with a non-inclined tool. The precipitation volume fraction of the base metal was equal to 3.557 pct and the FSW process resulted in a reduction of up to 1.285 pct. Due to the higher heat input during the process with the inclined tool, this effect was magnified. A revolutionary pitch parameter was introduced to determine the number of revolutions of the tool per 1 mm of its feed. As the value of revolutionary pitch and thus the amount of heat input increases, the precipitate volume fraction decreases due to an increase in their solubility. The maximum reduction of the precipitate volume fraction equal to 64 pct compared to the base material was found for the weld produced with the tool traverse speed of 200 mm/min, tool rotational speed of 1250 RPM and the tool tilt angle of 2 deg
4. The Williamson–Hall analysis was used to calculate residual strains. In addition, the indentation tests conducted allowed the calculation of residual stresses. Higher tensile residual stresses of -89.09 ± 6.19 MPa were observed in the parent material. The FSW process resulted in a reduction of the residual stresses up to -37.07 ± 2.94 MPa, which was particularly observed in the welds produced with the inclined tool.
5. The modified Williamson–Hall analysis was used to calculate the density and type of dislocation. The FSW process results in an increase in the fraction of dislocation of edge character dominating that had higher mobility. The sample produced with the tool rotational speed of 1000 RPM, tool traverse speed of 200 mm/min and the inclined tool was characterized by the dominance of edge character of dislocations of 71.3 pct while in the base material this value was equal to 18.2 pct. The change of the dislocation character influenced the dislocation mobility and it differed from 3.19×10^{-7} m/s for the base metal to 16.78×10^{-7} m/s for the weld produced with the tool rotational speed of 1000 RPM, traverse speed of 250 mm/min and the tool tilt angle of 2 deg.
6. Based on the calculations performed, the dislocation density was found to decrease for FSW welds up to the value of $1.419 \times 10^{13} \frac{1}{\mathrm{m}^2}$. The dislocation

density of the base metals was equal to 8.225×10^{13} $\frac{1}{m^2}$.

7. A parameter for the density of dislocations divided by their mobility was introduced. A linear decreasing relationship was observed between this parameter and the value of revolutionary pitch for both tool tilt angles. As the density of dislocations increases and their mobility decreases, higher weld strength is expected. Based on the analysis, the introduction of less heat was found to be more favorable. Also, the lower heat input during the process results in reduced dissolution of precipitates, which in the case of precipitate-strengthened alloys such as AA6082 is crucial with regard to their strength.

CONFLICT OF INTEREST

The authors declare that they have no conflict of interest.

OPEN ACCESS

REFERENCES

1. A. Laska and M. Szkodo: *Materials (Basel)*, 2020, vol. 13, pp. 1–46.
2. A.R.S. Essa, M.M.Z. Ahmed, A.K.Y.A. Mohamed, and A.E. El-Nikhaily: *J. Mater. Res. Technol.*, 2016, vol. 5, pp. 234–40.
3. M. Ilangovan, S.R. Boopathy, and V. Balasubramanian: *Def. Technol.*, 2015, vol. 11, pp. 174–84.
4. P. Cavaliere: *Procedia CIRP*, 2013, vol. 11, pp. 139–44.
5. S. Mabuwa and V. Msomi: *J. Mater. Res. Technol.*, 2020, vol. 9, pp. 9632–44.
6. A. Tamadon, D.J. Pons, K. Sued, and D. Clucas: *Metals (Basel)*, 2018, vol. 8, pp. 1–20.

F. Baratzadeh, E. Boldsaikhan, R. Nair, D. Burford, and H. Lankarani: *J. Adv. Join. Process.*, 2020, vol. 1, pp. 1–7.

P. Asadi, M.K.B. Givi, and M. Akbari: *Int. J. Adv. Manuf. Technol.*, 2016, vol. 83, pp. 301–11.

O. Barooni, M. Abbasi, M. Givi, and B. Bagheri: *Int. J. Adv. Manuf. Technol.*, 2017, vol. 93, pp. 4371–78.

N.M. Daniolos and D.I. Pantelis: *Int. J. Adv. Manuf. Technol.*, 2017, vol. 88, pp. 2497–2505.

11. A. Laska, M. Szkodo, D. Koszelow, and P. Cavaliere: *Metals (Basel)*, 2022, vol. 12, pp. 1–6.
12. A.H. Feng, B.L. Xiao, and Z.Y. Ma: *Compos. Sci. Technol.*, 2008, vol. 68, pp. 2141148.
13. J.F. dos Santos, P. Staron, T. Fischer, J.D. Robson, A. Kostka, P. Colegrove, H. Wang, J. Hilgert, L. Bergmann, L.L. Hütsch, N. Huber, and A. Schreyer: *Acta Mater.*, 2018, vol. 148, pp. 163–72.
14. P. Thirathipviwat, G. Song, J. Bednarcik, U. Kühn, T. Gemming, K. Nielsch, and J. Han: *Prog. Nat. Sci. Mater. Int.*, 2020, vol. 30, pp. 545–51.
15. Z. Zhuang, Z. Liu, and Y. Cui: *Dislocation Mechanism-Based Crystal Plasticity Theory and Computation at the Micron and Submicron Scale*, Elsevier Inc., 2019.
16. P.B. Prangnell and C.P. Heason: *Acta Mater.*, 2005, vol. 53, pp. 3179–92.
17. Z. Gao, J. Feng, Z. Wang, J. Niu, and C. Sommitsch: *Metals (Basel)*., DOI:https://doi.org/10.3390/met9060672.
18. W. Woo, L. Balogh, T. Ungár, H. Choo, and Z. Feng: *Mater. Sci. Eng. A*, 2008, vol. 498, pp. 308–13.
19. W. Woo, T. Ungár, Z. Feng, E. Kenik, and B. Clausen: *Metall. Mater. Trans. A*, 2010, vol. 41, pp. 1210–16.
20. D. Yuzbekova, V. Kulitskiy, A. Mogucheva, and R. Kaibyshev: *Mater. Sci. Forum*, 2017, vol. 879, pp. 2249–54.
21. W.B. Lee and S.B. Jung: *Mater. Lett.*, 2004, vol. 58, pp. 1041–46.
22. J. Altenkirch, A. Steuwer, M.J. Peel, P.J. Withers, S.W. Williams, and M. Poad: *Metall. Mater. Trans. A*, 2008, vol. 39, pp. 3246–59.
23. Y. Lin: *Recent Advances in Structural Integrity Analysis - Proceedings of the International Congress (APCF/SIF-2014)*, Woodhead Publishing, 2014.
24. W. Chen, G. Van Boven, and R. Rogge: *Acta Mater.*, 2007, vol. 55, pp. 43–53.
25. T. Li, Q.Y. Shi, and H.K. Li: *Sci. Technol. Weld. Join.*, 2007, vol. 12, pp. 664–70.
26. L.Y. Bai, L. Gao, and K.B. Jiang: *IOP Conf. Ser. Mater. Sci. Eng.*, 2018, vol. 21, pp. 1–10.
27. A. Laska, M. Szkodo, Ł. Pawłowski, and G. Gajowiec: *Int. J. Precis. Eng. Manuf. Green Technol.*, https://doi.org/10.1007/s40684-022-00441-z.
28. M. Peel, A. Steuwer, M. Preuss, and P.J. Withers: *Acta Mater.*, 2003, vol. 51, pp. 4791–4801.
29. R. John, K.V. Jata, and K. Sadananda: *Int. J. Fatigue*, 2003, vol. 25, pp. 939–48.
30. A. Steuwer, M.J. Peel, and P.J. Withers: *Mater. Sci. Eng. A*, 2006, vol. 441, pp. 187–96.
31. C. Zhang and A.A. Shirzadi: *Sci. Technol. Weld. Join.*, 2018, vol. 23, pp. 394–99.
32. M. Szkodo, A. Bień, and A. Stanisławska: *Int. J. Precis. Eng. Manuf. - Green Technol.*, 2022, vol. 9, pp. 175–90.
33. R.A. Young: *The Rietveld Method*, International Union of Crystallography, 1995.
34. M.D. Sandar and S. Yasasvi: *Int. J.*, 2017, vol. 3, pp. 39–47.
35. A. Abdollahzadeh, B. Bagheri, M. Abassi, A.H. Kokabi, and A.O. Moghaddam: *J. Mater. Eng. Perform.*, 2021, vol. 30, pp. 1110–27.
36. N. Dialami, M. Cervera, and M. Chiumenti: *Metals (Basel)*, 2019, vol. 9, pp. 1–7.
37. B. Bagheri, M. Abbasi, and M. Dadaei: *J. Mater. Eng. Perform.*, 2020, vol. 29, pp. 1165–75.
38. J. Chen, W. Yan, C.X. Liu, R.G. Ding, and X.H. Fan: *Mater. Charact.*, 2011, vol. 62, pp. 237–42.
39. A. Lehtinen, L. Laurson, F. Granberg, K. Nordlund, and M.J. Alava: *Sci. Rep.*, 2018, vol. 8, pp. 1–2.
40. C.V. Rao, G.M. Reddy, and K.S. Rao: *Def. Technol.*, 2015, vol. 11, pp. 197–208.
41. G.G. Krishna, P.R. Reddy, and M.M. Hussain: *Glob. J. Res. Eng.*, 2014, vol. 14, pp. 61–70.
42. S.D. Meshram and G.M. Reddy: *Def. Sci. J.*, 2018, vol. 68, pp. 512–18.
43. G.K. Williamson and W.H. Hall: *Acta Metall.*, 1953, vol. 1, pp. 22–31.
44. P. Scherrer: Bestimmung Der Inneren Struktur Und Der Größe von Kolloidteilchen Mittels Röntgenstrahlen, in *Kolloidchemie Ein Lehrbuch*. R. Zsigmondy, ed., Springer, Berlin, 1912.
45. M.S. Khoshkhoo, S. Scudino, J. Thomas, K.B. Surreddi, and J. Eckert: *J. Alloys Compd.*, 2011, vol. 509, pp. S343-47.

46. F. HajyAkbary, J. Sietsma, A.J. Böttger, and M.J. Santofimia: *Mater. Sci. Eng. A*, 2015, vol. 639, pp. 208–18.
47. T. Ungár, I. Dragomir, Á. Révész, and A. Borbély: *J. Appl. Crystallogr.*, 1999, vol. 32, pp. 992–1002.
48. J. Vallin, M. Mongy, K. Salama, and O. Beckman: *J. Appl. Phys.*, 1964, vol. 35, pp. 1825–26.
49. S.S. Bargujer, N.M. Suri, and R.M. Belokar: *Def. Sci. J.*, 2015, vol. 65, pp. 500–07.
50. W.J. Poole and D.J. Lloyd: *Proc. 9th Int. Conf. Alum. Alloy.*, 2004, pp. 939–45.
51. S.R. Valvi, A. Krishnan, S. Das, and R.G. Narayanan: *Int. J. Mater. Form.*, 2016, vol. 9, pp. 115–29.
52. U. Messerschmidt, B.V. Petukhov, M. Bartsch, C. Dietzsch, B. Geyer, D. Häussler, L. Ledig, M. Feuerbacher, P. Schall, and K. Urban: *Mater. Sci. Eng. A*, 2001, vol. 319–321, pp. 107–10.
53. C.T. Mouni, M.S.R.C.S.K. Albert, C.R. Das, P.K. Parida, and A. Sagdeo: *Mater Sci. Eng. A*, 2021, vol. 826, p. 141960.
54. E. Schafler, M. Zehetbauer, and T. Ungàr: *Mater. Sci. Eng. A*, 2001, vol. 319–321, pp. 220–23.
55. T.H. Simm: *Crystals*, 2018, vol. 8, pp. 1–32.
56. B. Chen, S. Li, H. Zong, X. Ding, J. Sun, and E. Ma: *Proc. Natl. Acad. Sci.*, 2020, vol. 117, pp. 16199–61206.
57. S. Starikov and V. Tseplyaev: *Comput. Mater. Sci.*, 2020, vol. 179, pp. 1–4.